2016-01-1599
Published 04/05/2016
Copyright © 2016 SAE International
doi:10.4271/2016-01-1599
saepcmech.saejournals.org

Adjoint-Driven Aerodynamic Shape Optimization Based on a Combination of Steady State and Transient Flow Solutions

Taeyoung Han, Shailendra Kaushik, and Kenneth Karbon
General Motors Co.

Benjamin Leroy, Kyle Mooney, Stamatina Petropoulou, and Jacques Papper
ICON Technology and Process Consulting Ltd.

ABSTRACT

Aerodynamic vehicle design improvements require flow simulation driven iterative shape changes. The 3-D flow field simulations (CFD analysis) are not explicitly descriptive in providing the direction for aerodynamic shape changes (reducing drag force or increasing the down-force). In recent times, aerodynamic shape optimization using the adjoint method has been gaining more attention in the automotive industry. The traditional DOE (Design of Experiment) optimization method based on the shape parameters requires a large number of CFD flow simulations for obtaining design sensitivities of these shape parameters. The large number of CFD flow simulations can be significantly reduced if the adjoint method is applied. The main purpose of the present study is to demonstrate and validate the adjoint method for vehicle aerodynamic shape improvements. Although steady-state Reynolds Averaged Navier Stokes (RANS) was used as a 'primal' solution for adjoint-based shape changes, a fully transient Detached Eddy Simulation (DES) was applied as the baseline and final flow solutions for improved flow accuracy. This type of analysis offers a more accurate flow modelling option, especially in cases where boundary layer separation occurs. The DES validation run was performed in the final stage of this study in order to confirm the drag coefficient reduction of $\Delta CD = -0.005$. The hardware validation results with a reduced scale clay model in a wind tunnel will be reported in future publications.

CITATION: Han, T., Kaushik, S., Karbon, K., Leroy, B. et al., "Adjoint-Driven Aerodynamic Shape Optimization Based on a Combination of Steady State and Transient Flow Solutions," *SAE Int. J. Passeng. Cars - Mech. Syst.* 9(2):2016, doi:10.4271/2016-01-1599.

INTRODUCTION

Computational Fluid Dynamics (CFD) has gained popularity as a tool for many airflow situations including road vehicle aerodynamics. This trend, to bring CFD to bear on vehicle aerodynamic design issues, is appropriate and timely in view of the increasing competitive and regulative pressures being faced by the automotive industry. Vehicle shape optimization for better aerodynamics performance is one of the most appealing ways of meeting these demands. The automatic optimization can be very beneficial in maintaining short vehicle production cycles. Conventional CFD flow information such as air velocity and pressure field do not provide direct guidance on the shape changes for improving the vehicle aerodynamic performance. This is because the 3-D flow field obtained from a standard CFD analysis is not explicitly descriptive to provide direct guidance on how changes to the vehicle shape impact the aerodynamic performance.

The adjoint method provides the design direction and the sensitivity information with only one solution of the adjoint equation, which is independent of the number of shape parameters. There is a long history of the use of the adjoint technique in CFD shape optimization with the major contributors being Jameson [1], Giles [2], Anderson [3] and others. More recent work from the authors on the adjoint solver in topology and shape optimization can be found in [4], [5] and [6]. The process involves only one conventional CFD simulation and one adjoint solution in which the sensitivity of aerodynamic drag with respect to the shape is extracted at every surface mesh location on the vehicle. An optimized vehicle shape based on the drag sensitivities is then obtained. Although the adjoint method has been used extensively in many aerodynamic optimization problems, its application to full-scale vehicle design is still very challenging. The design engineers have to determine whether the suggested shape changes from the adjoint method are adequate to provide improved drag. At the same time, these changes must not conflict with other design constraints such as the interior volume, comfort, styling, various safety requirements and functionality.

The baseline vehicle shape was a production vehicle, already optimized using wind-tunnel testing and standard CFD processes at GM. The study is arranged in two phases. In phase 1, the optimization module was used to automatically loop through the primal-adjoint-morph steps, to reduce drag. In phase 2, a manual approach to optimization, especially developed for this investigation was adopted. In this approach, six potentially beneficial regions on the car surface (Figure 1) were identified using the adjoint sensitivity plots. From the pre-processing to the solver stages, every operation

described in this paper has been completed using iconCFD®[7] software developed by ICON Technology and Process Consulting Ltd®. These were sequentially morphed, one zone at a time, using the box-morphing toolset available in ANSA® [8]. This enabled larger surface deformations while maintaining smoothness and integrity of the morphed surfaces in the identified regions which was not possible in phase 1 approach.

ADJOINT EQUATIONS

The adjoint method is used for the calculation of the shape sensitivities of the vehicle. The adjoint equations implemented in the software are given in [9]-[10]. The required source terms and the adjoint boundary conditions are formulated as functions of the fluid dynamic objectives. The main equations of [10] are briefly outlined here. In this case, the porosity term is omitted from the adjoint momentum equation since the interest is in the surface sensitivities and no topology optimization is taking place. Assuming a generalized cost function, J, on the computational domain, Ω:

$$J = J(\mathbf{v}, p) = \int_{\Gamma} J_{\Gamma} d\Gamma + \int_{\Omega} J_{\Omega} d\Gamma, \qquad \Gamma = \partial\Omega \ \ or\ part\ of\ \partial\Omega$$

Where J_Γ is the surface contribution of the cost function and J_Ω is the volume part. $\mathbf{v}$ is the primal velocities and p is the primal pressure field.

- The steady-state, incompressible Navier-Stokes adjoint equations with frozen turbulence takes the form:

$$-2D(\mathbf{u})\mathbf{v} = -\nabla q + \nabla \cdot \left(2\nu D(\mathbf{u})\right) - \frac{\partial J_{\Omega}}{\partial \mathbf{v}}$$

$$\nabla \cdot \mathbf{u} = \frac{\partial J_{\Omega}}{\partial p}$$

$$where \quad 2D(\mathbf{u})\mathbf{v} = -\nabla \mathbf{u} \cdot \mathbf{v} - (\mathbf{v} \cdot \nabla)\mathbf{u}$$

- The adjoint boundary conditions for walls and inlets are:

$$\mathbf{u}_t = 0$$

$$\mathbf{u}_n = -\frac{\partial J_{\Gamma}}{\partial p}$$

- The adjoint boundary conditions for outlets are:

$$q = \mathbf{u} \cdot \mathbf{v} + \mathbf{u}_n \mathbf{v}_n + \nu \left(\mathbf{n} \cdot \nabla\right)\mathbf{u}_n + \frac{\partial J_{\Gamma}}{\partial \mathbf{v}_n}$$

$$0 = \mathbf{u} \cdot \mathbf{v} + \mathbf{u}_n \mathbf{v}_n + \nu \left(\mathbf{n} \cdot \nabla\right)\mathbf{u}_t + \frac{\partial J_{\Gamma}}{\partial \mathbf{v}_t}$$

- The sensitivity derivatives with respect to an outward movement, β, on the surface have the following form with A being the surface area affected by this movement:

$$\frac{\partial L}{\partial \beta} = -A\nu \left(\mathbf{n} \cdot \nabla\right)\mathbf{u}_t \cdot \left(\mathbf{n} \cdot \nabla\right)\mathbf{v}_t$$

$$where \qquad L = J + \int_{\Omega} (\mathbf{u}, q) R d\Omega,$$

R stands for the residuals of the Navier-Stokes equations, $\mathbf{n}$ is the unit normal vector, $\mathbf{v}$ and $\mathbf{u}$ are the primal and adjoint velocities respectively, p and q are the primal and adjoint pressures respectively and ν is the kinematic viscosity. The subscript n and t represent the normal and tangential component of a field respectively.

The cost function used for the measurement of the drag forces reduction was:

$$J = \int_{S} \mathbf{d} \cdot \left(\mathbf{n}p - \nu \frac{d\mathbf{v}}{\delta n} \right) ds, \qquad \begin{cases} d = (1,0,0) \ for\ drag \\ d = (0,0,1) \ for\ lift \end{cases}$$

where S is usually the car surface. The definition of the cost function is such that only the pressure component of the drag is taken into account for the optimization. Since the pressure component is dominant, this definition is adequate.

SOLUTION METHODOLOGY

A spreadsheet based preprocessing tool (iconCFD MultiCase©) was used to quickly prepare a number of simulation cases, ready for submission using STL geometry assemblies and user-defined templates (e.g. wind tunnel for automotive applications). The optimization process was divided into two phases:

Phase 1

In the first phase, the exterior of the vehicle was morphed through an iterative optimization process. Some geometry preparations were initially required to group geometry patches together in order to control morphing and the drag coefficient improvements (monitored between each cycle). The optimization consisted of a RANS flow run also called the “primal” run, an adjoint run where the sensitivities were computed, and a morphing stage. The direct deformation morpher works as follows: the sensitivities are translated into point displacement and scaled back to restrict the deformation to a given maximum displacement, followed by further smoothing. The morphing is applied on the geometry triangulated grid and exported in STL format in order to be used in the subsequent optimization steps. The normalized sensitivities (scalar values) are used in the morphing, and the local surface displacements are proportional to the local sensitivity vectors (“push in” or “pull out”). During the first phase, the shape sensitivities were applied to the entire vehicle surface and the total drag improvement due to the shape change evaluated. The maximum allowed displacement is defined by the user and the effects of the shape change on the total drag coefficients is investigated.

Phase 2

In the second phase, the exterior surfaces that demonstrated the highest sensitivities were selected for individual sub-region optimization, as shown in Figure 1. The optimization process exploited a "front-to-rear" approach (the direction in which the morphing takes place), where each subsequent run used the previous sub-section geometry modification. A flow simulation followed by an adjoint sensitivity simulation was then performed for each configuration.

During the second phase, surface morphing was applied using the CAD pre-processing tool in which morphing boxes were created around each sub-region. The morphed geometry from the first phase was used as a guide for the individual sub-region morphing. The morphing boxes were introduced in such a way that the symmetry of the end design was preserved (see Figure 2).

Certain geometric constraints were introduced during the CAD software morphing process; for example, the mirror glass surface was unchanged (see Figure 3).

For each sub-region morphing, the drag improvements were recorded by RANS simulations. Although RANS simulations tend to predict the drag increments due to shape changes, DES simulations are considered more accurate for the overall drag predictions. Therefore, in order to confirm the total drag reduction, DES confirmation runs were performed on the original and fully morphed designs after the completion of the second phase.

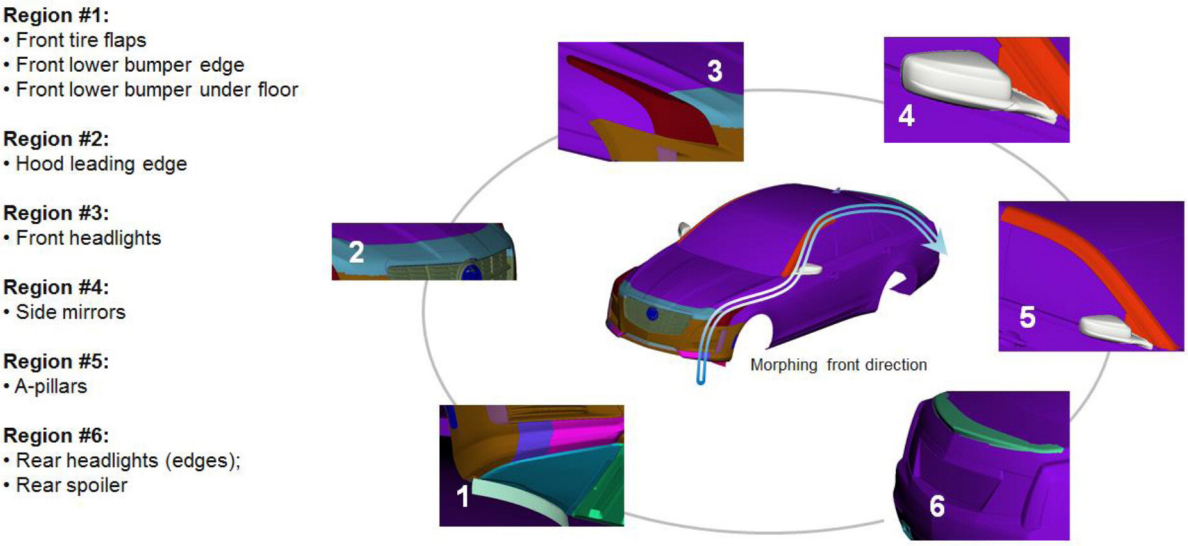


Figure 1. Selected areas for local optimization

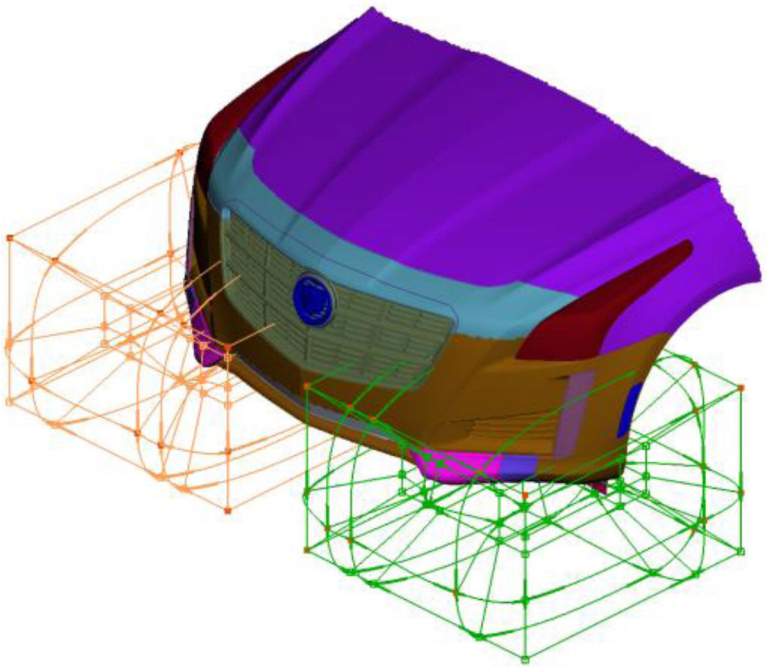


Figure 2. Example of the morphing boxes around the front bumper.

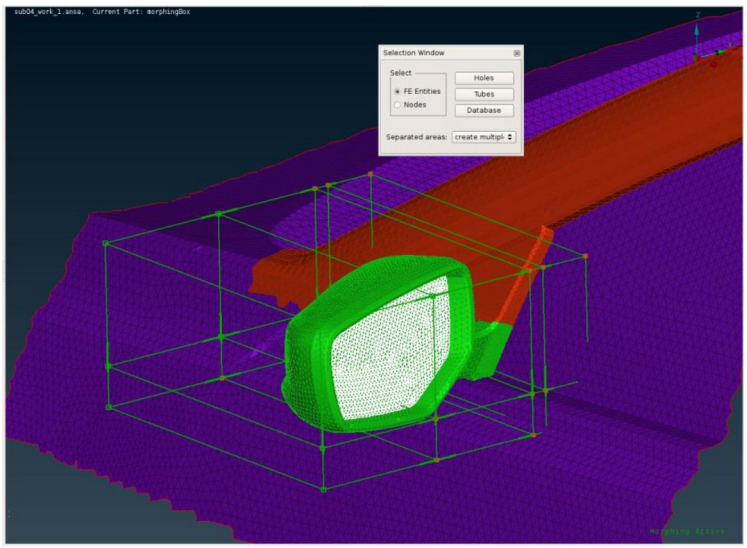


Figure 3. Introducing morphing constraints through the CAD software. Constrained mirror surface.

RESULTS

All cases presented in this study were completed on a GM production vehicle as seen in Figure 4. As the focus is on external aerodynamic changes, the under-hood compartment was closed with a surface on the front grille. For the computational domain, a standard wind tunnel model as represented in Figure 5 was used. The main boundary conditions are presented in Table 1.

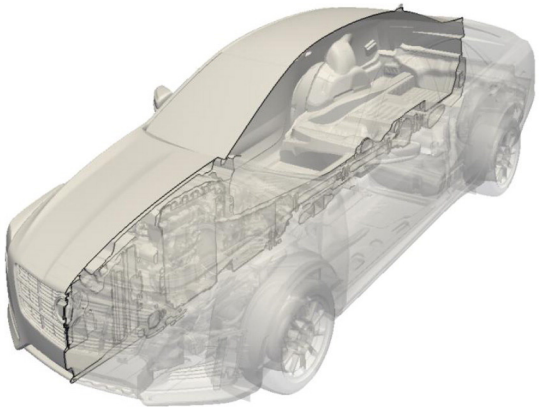


Figure 4. Car CAD model with closed under-hood compartment.

Figure 6 shows the vehicle geometry and the velocity field in the symmetry plane. A predominantly polyhedral mesh with prism layers at the walls has been used in the primal flow and the adjoint simulations. Wall Y+ distribution on the main external aerodynamic surfaces of the car are within a range of [30-40]. In the second phase, more detailed analysis was required due to the local areas of interest, so further refinement of the surface and overall mesh was applied in phase 2. This led to a mesh size (in the second phase) to approximately 85M cells compared to 26M cells in the first phase. A RANS, steady state solver with the Realizable k-ε model [11] was used for the drag calculations between optimization loops.

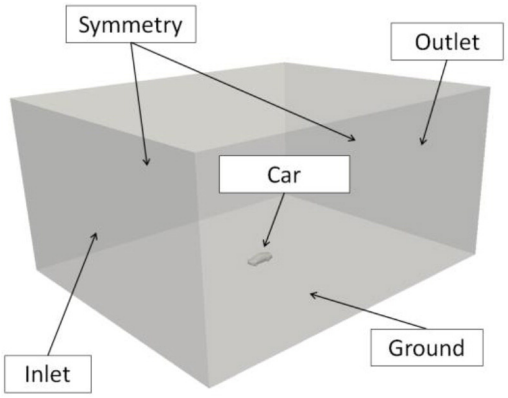


Figure 5. Wind tunnel setup

Table 1. Boundary conditions description

Part ID	Boundary condition types
Inlet	Velocity inlet (30m/s)
Outlet	Pressure outlet
Ground	Static wall
Car body	Static wall
Car wheels	Static wall

For phase 1, the whole exterior styling was modified during three consecutive optimization iterations. The drag coefficients as well as the changes in frontal area can be seen in Table 2. For this phase the process was fully automated. Simulations were considered converged when the drag coefficient oscillations reached an amplitude of 0.5drag count.

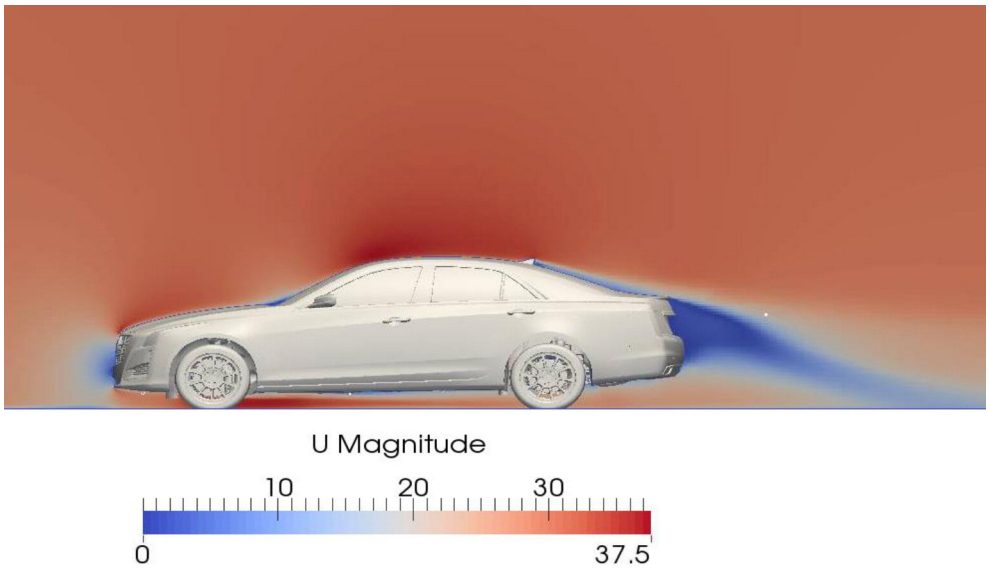


Figure 6. RANS solver velocity field y=0 cut.

Table 2. Phase 1 - Drag coefficient reduction during iterations.

Case ID	Area modified	ΔCd (1 count=0.001)	Frontal Area (m^2)
Original (Baseline)	Base	-	2.321
Morphed 1	Exterior styling	-3.6	2.312
Morphed 2	Exterior styling	-3.8	2.305
Morphed 3	Exterior styling	-3.5	2.299

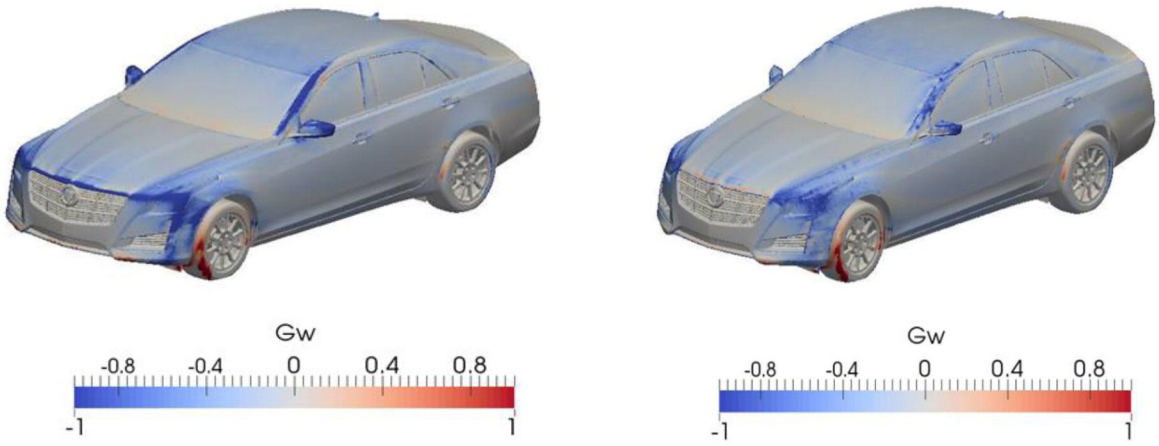


Figure 7. Phase 1 - Comparison of original (left) and final (right) sensitivities.

As the geometries was morphed, the frontal area changed (see Table 2 and Table 4) and in order to consistently compare the drag coefficients a constant reference frontal area of 2.321m^2 was used (original geometry frontal area value).

The surface sensitivities of the baseline versus the last design can be seen in Figure 7. The strength of the shape sensitivity was softened from the baseline shape to the final morphed shape. A total drag reduction of 3.8 counts was achieved in this phase. The maximum displacement was limited to 20 mm for each optimization iteration and to 30 mm for the overall optimization process. The areas that reached the overall maximum displacement of 30 mm were excluded from the next optimization iteration. The maximum of 30 mm was achieved in some of the most deformed areas. The relatively small

drag reduction for 30 mm of maximum displacement is due to the fact that the direct deformation morpher produced some rough surfaces on the exterior of the car.

The shape sensitivities predicted from the baseline (as shown in Figure 7) were utilized to select 6 sub-regions to be optimized in the second phase using the manual deformation optimization process. The selection of the 6 sub-regions was based on the strength of the sensitivities around the entire vehicle as shown in Figure 7 for the original shape. The different sub-regions were run cumulatively from the front to the rear of the car, as shown in Figure 1. For the morphing of each region in phase 2, the morphing boxes were generated with the CAD pre-processing tool box. The manual morphing boxes can directly influence the magnitude of the shape changes and also produce a very smooth surface geometry compared to the automatic morphing process applied in phase 1. The maximum displacements for each sub-region were are shown in Table 3.

In Table 4, the drag reduction for each sub-region is summarized, in which a consistent drag reduction is observed on cumulative designs. It is apparent that the frontal area was not significantly reduced in most regions with the exception of the mirrors. The overall drag reduction was 9.1 counts. This has been obtained after averaging drag values over the last 500 iterations (in the same way that the drag coefficient has been calculated for all other RANS cases).

The method described in the previous section involving the morphed geometry of phase 1 and the CAD preprocessing tool morphing techniques was used to deform each sub-region. The morphing of each sub-region can be seen in Figure 8 to Figure 13. Original and morphed geometries pictures are shown alongside of the overlaid geometries. Designs of new non-intuitive morphing such as the strake between the lower bumper edge and the tire flap were directly guided by the trends suggested by the phase 1 morphed geometry (see Figure 8). The deltas between the original and the morphed geometry for the development of the lift and drag coefficients and their local contribution are compared in Figure 14 and Figure 15 respectively. In Figure 16 the difference between the original (left) and morphed (right) velocity fields are compared on x and y slices and show a reduction in the wake which can explain the drag reduction. Differences are subtle but one will notice the regions of recirculation near the ground and in the symmetry plane are slightly narrower in the morphed case. The surface sensitivity intensity has significantly reduced after the completion of phase 2 demonstrating that the morphing has driven the shape towards a local optimum (Figure 17).

Table 3. Summary of maximum displacement for each sub-region using hybrid morphing.

Case ID	Area modified	Max. Normal Displacement (mm)
Original	NA	15
Sub-Region 1	tire flap + lower bumper	10
Sub-Region 2	hood leading edge	20
Sub-Region 3	headlights	8
Sub-Region 4	side mirrors	8
Sub-Region 5	A-pillars	10
Sub-Region 6	rear lights + spoiler	15

Table 4. Phase 2 - Drag reduction information for each sub-region.

Case ID	Area modified	ΔCd between shape changes (count)	ΔCd accumulated (count)	Frontal Area (m^2)
Original	NA	-	-	2.321
Sub-Region 1	tire flap + lower bumper	-2.6	-2.6	2.319
Sub-Region 2	hood leading edge	-0.7	-3.3	2.319
Sub-Region 3	headlights	-0.4	-3.7	2.319
Sub-Region 4	side mirrors	-0.9	-4.6	2.318
Sub-Region 5	A-pillars	-0.1	-4.7	2.318
Sub-Region 6	rear lights + spoiler	-4.4	-9.1	2.318

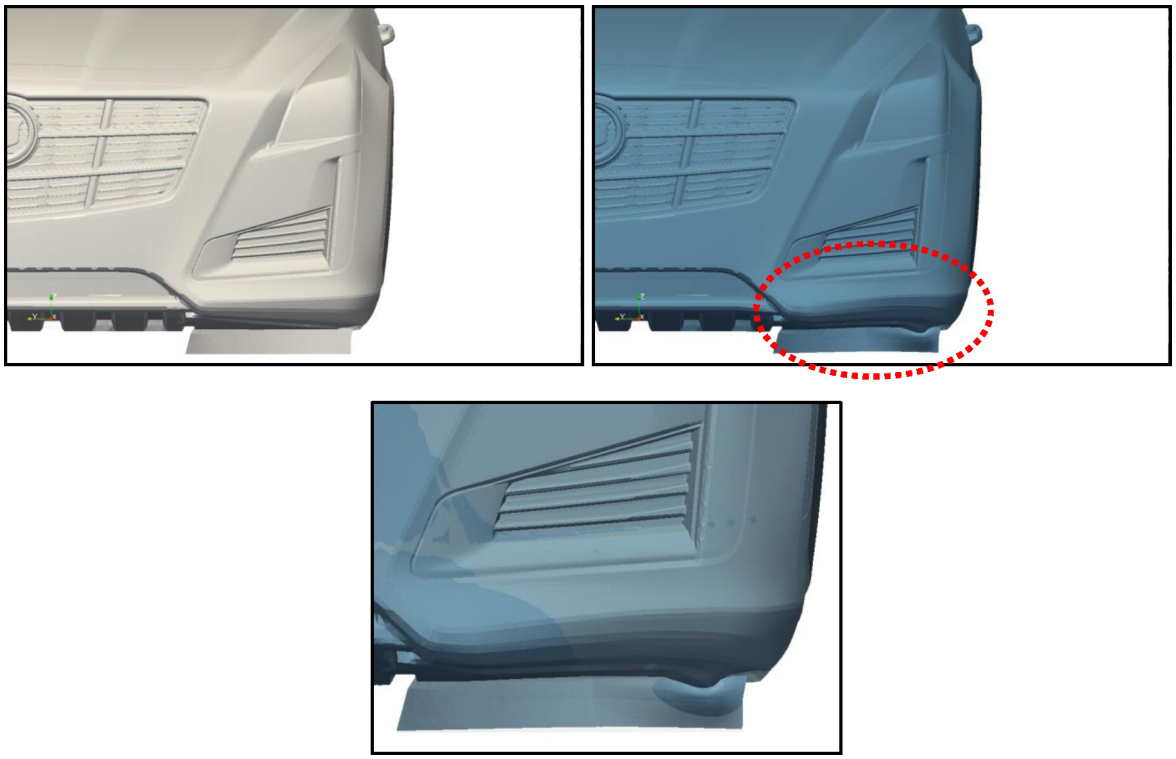


Figure 8. Baseline vs. morphed geometry of sub-region 1, tire flap + lower bumper. Overlaid geometries with baseline in grey transparency.

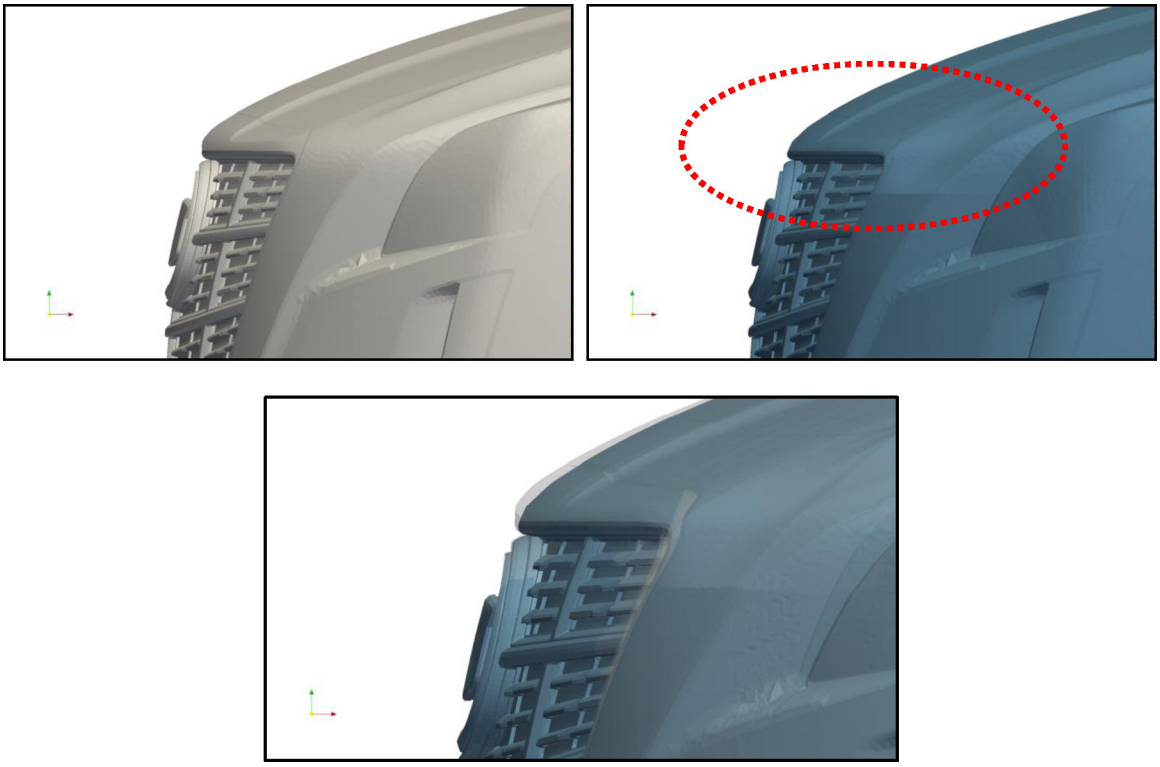


Figure 9. Baseline vs. morphed geometry of sub-region 2, hood leading edge. Overlaid geometries with baseline in grey transparency.

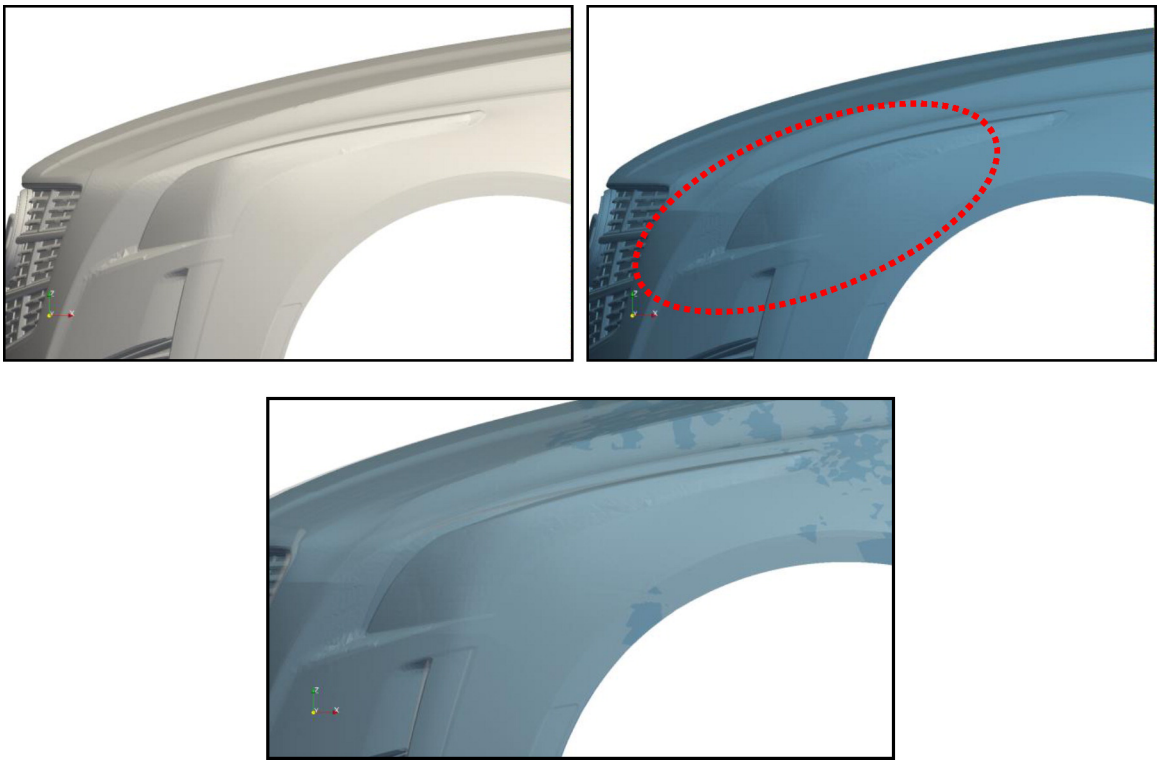


Figure 10. Baseline vs. morphed geometry of sub-region 3, headlights. Overlaid geometries with baseline in grey transparency.

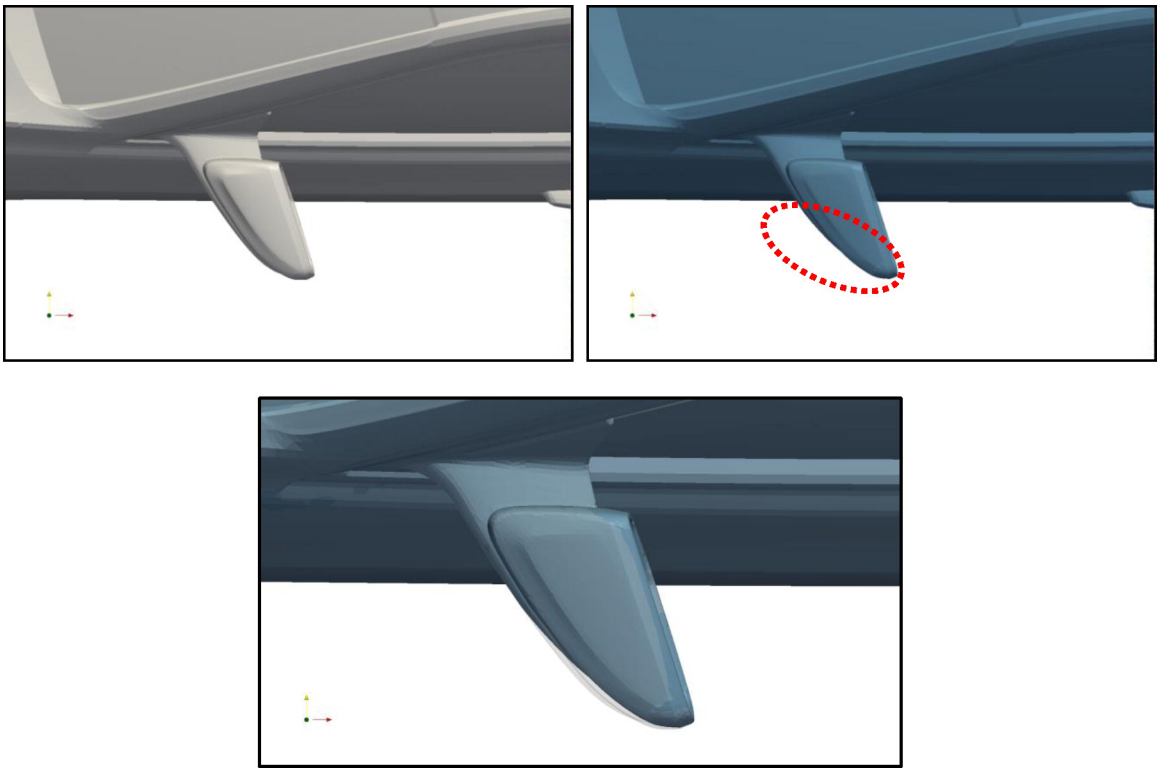


Figure 11. Baseline vs. morphed geometry of sub-region 4, side mirrors. Overlaid geometries with baseline in grey transparency.

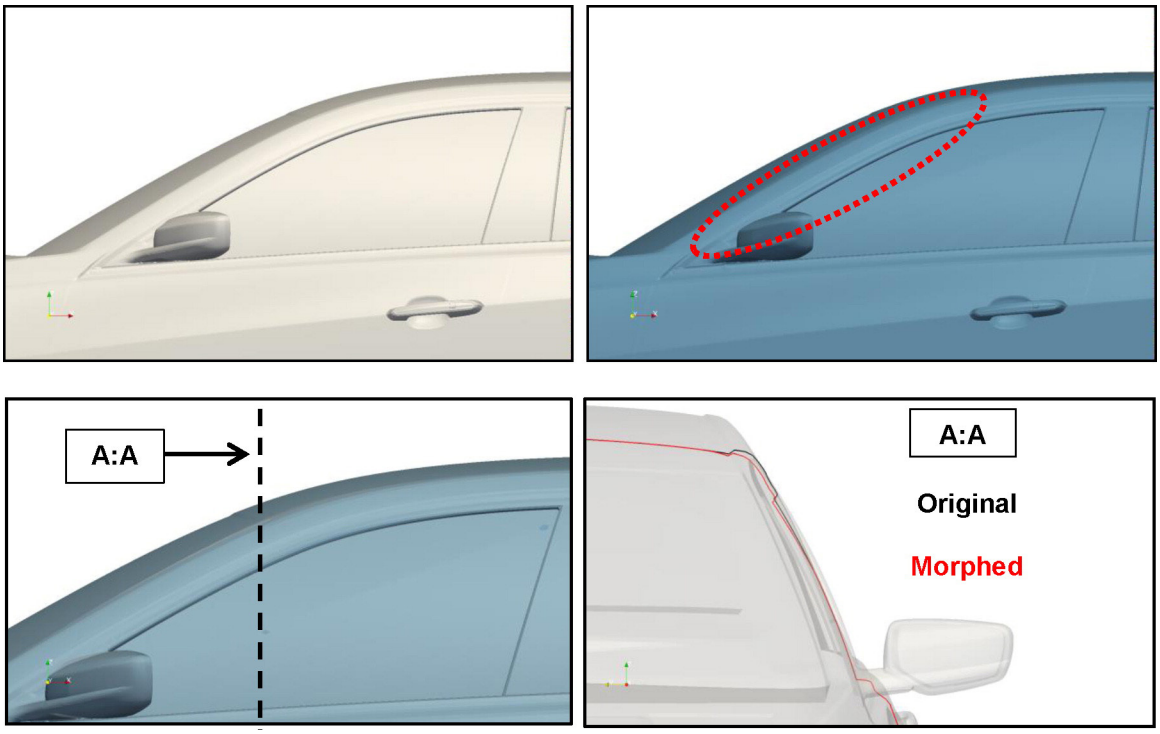


Figure 12. Baseline vs. morphed geometry of sub-region 5, A-pillars. Overlaid geometries with baseline in grey transparency and X-cuts.

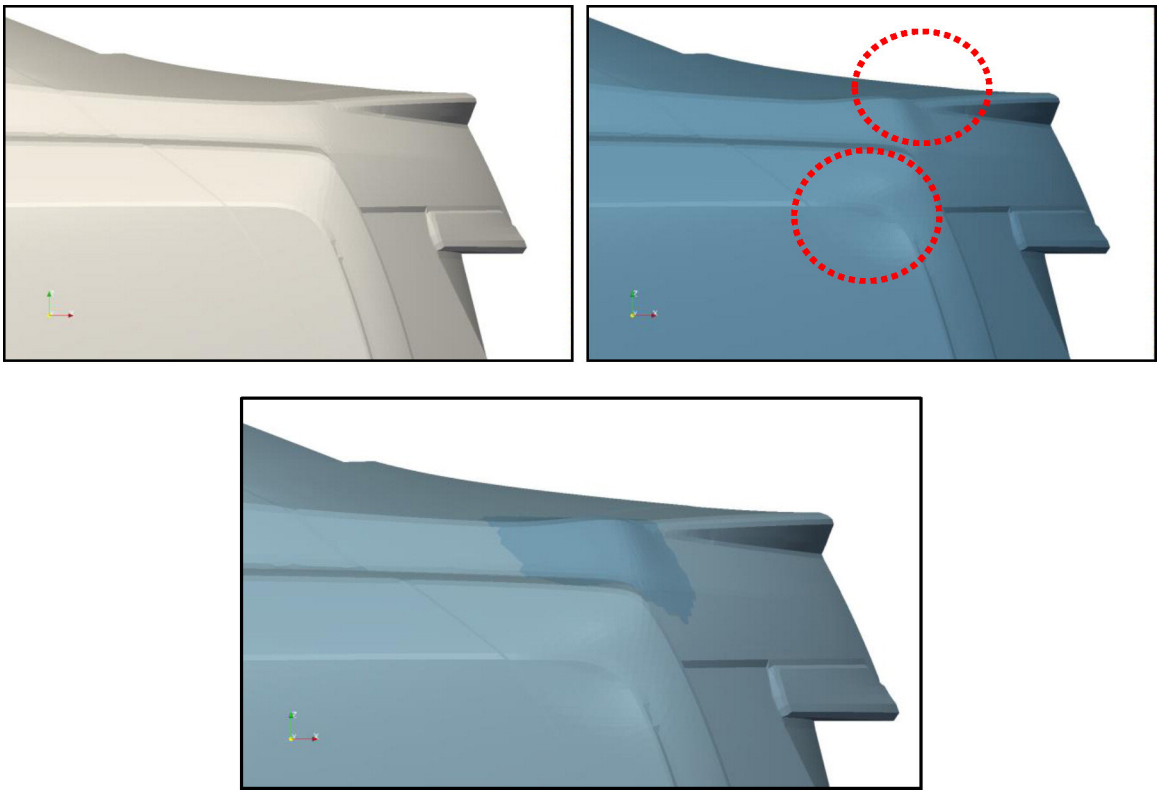


Figure 13. Baseline vs. morphed geometry of sub-region 6, rear lights + spoiler. Overlaid geometries with baseline in grey transparency.

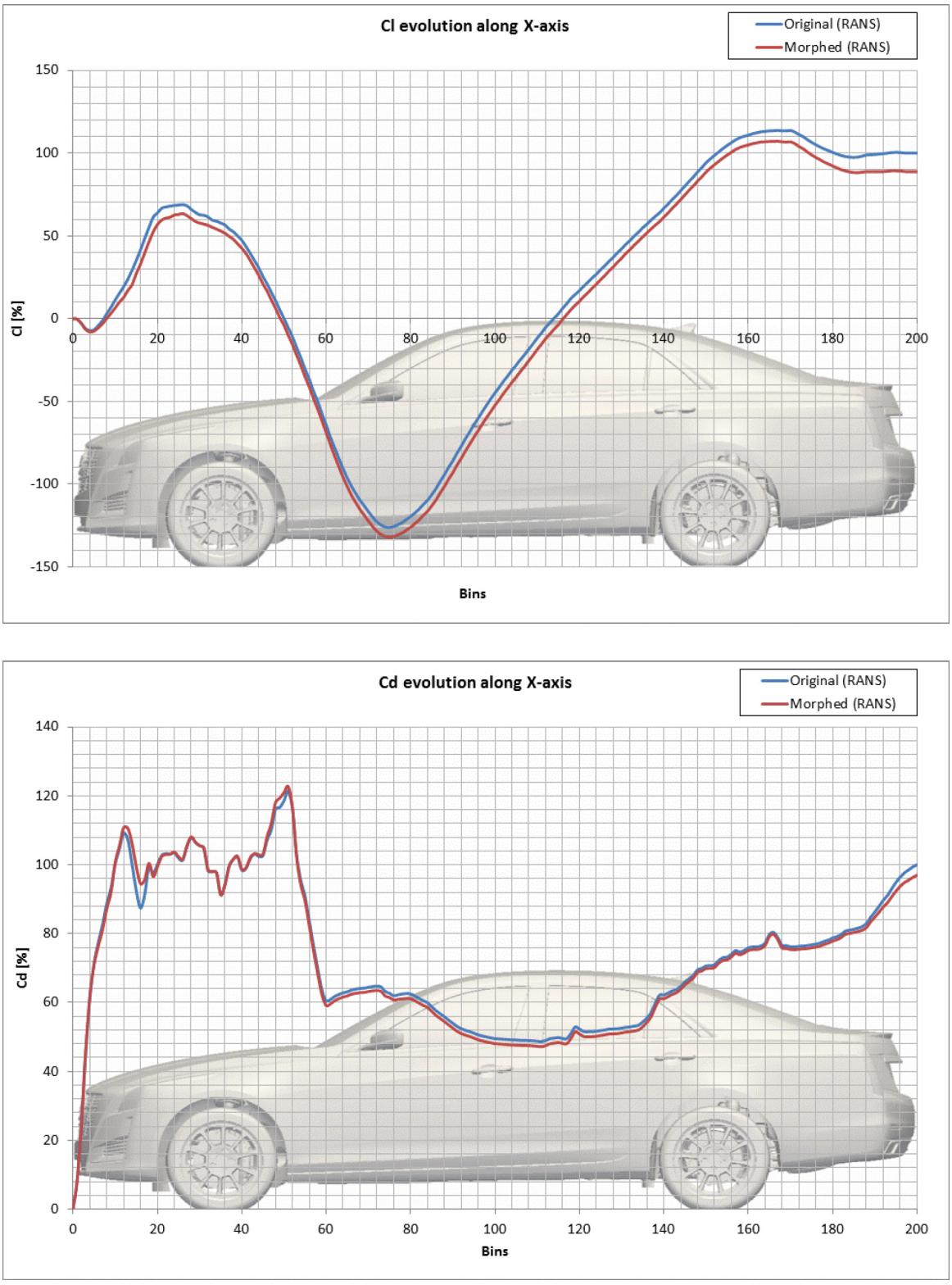


Figure 14. Lift (top) and drag (bottom) bin distribution comparison of the original and morphed geometry.

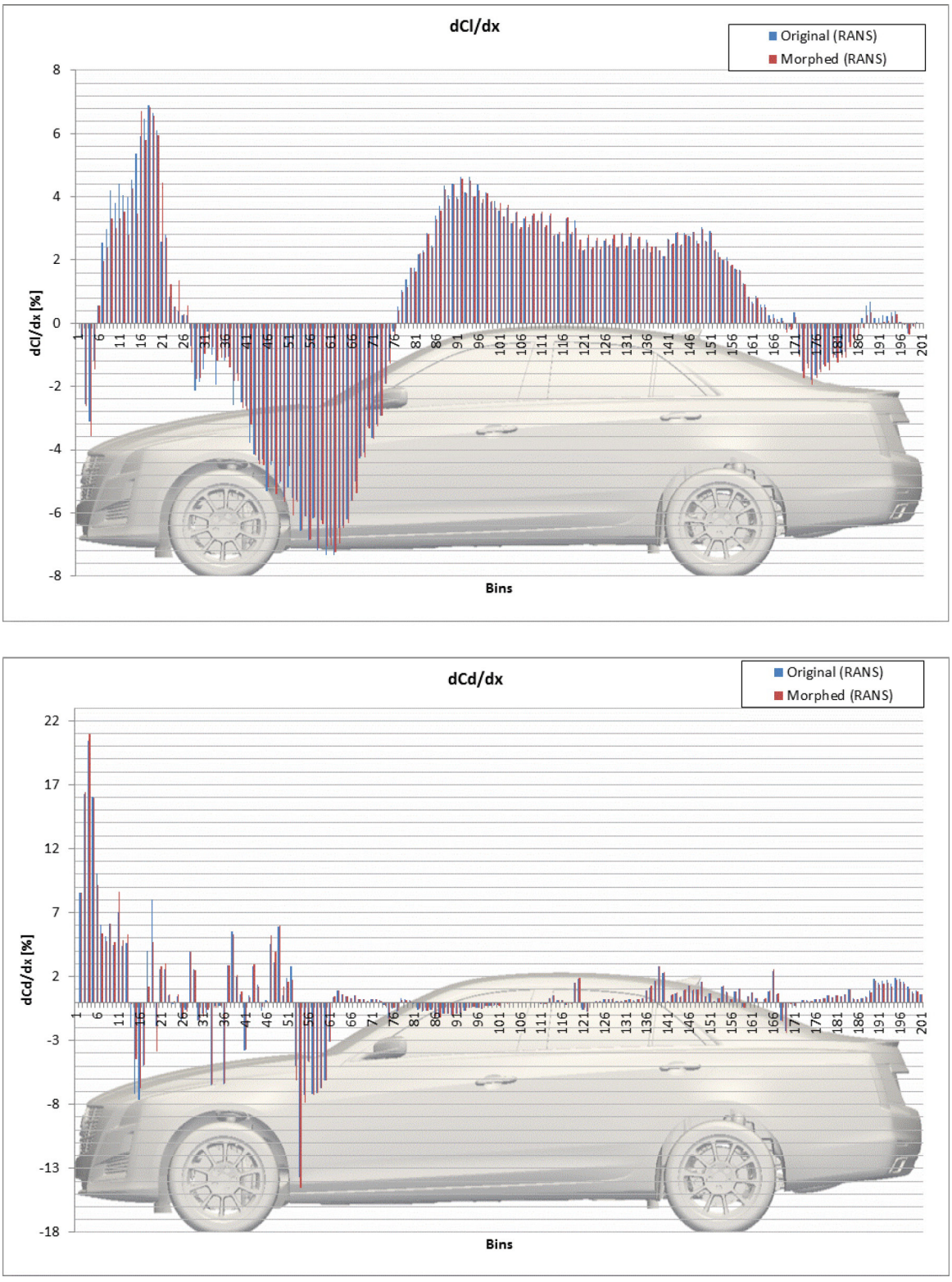


Figure 15. Lift (top) and drag (bottom) delta bin distribution comparison of the original and morphed geometry.

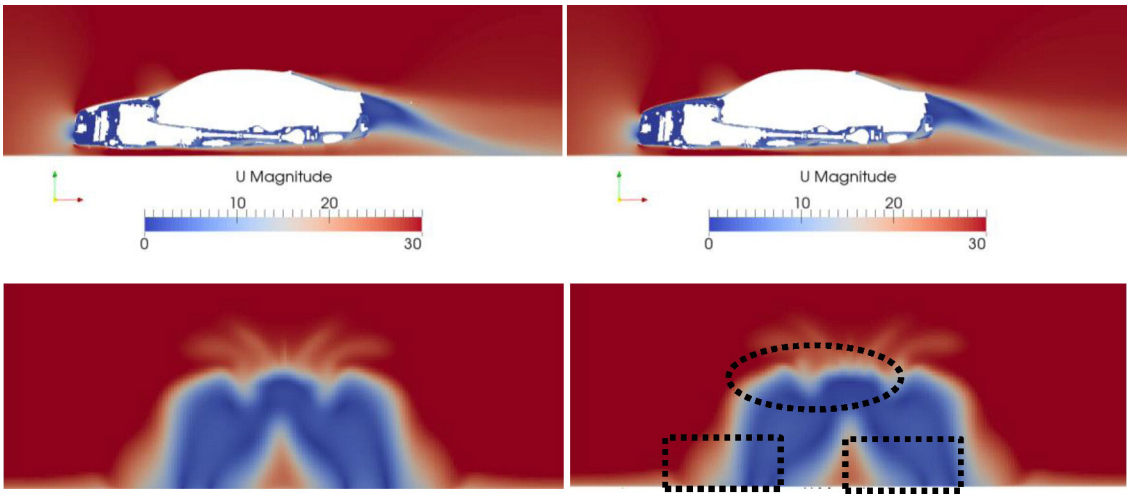


Figure 16. Comparison of velocity fields between original (left) and morphed (right) geometries. Top y=0 cut. Bottom x=5.2 slice (position of largest wake difference between two cases).

For the DES validation, a coarse-to-fine approach was adopted to initialize the solution with a coarse mesh solution mapped onto a fine mesh in order to save the computational time costs. A different time step was used for each mesh in order to maintain a low value for the maximum Courant number (~ 4). The case run for a total simulation time of 3.0 seconds (1.5 seconds for the coarse + 1.5 seconds for the fine case). The instantaneous velocity field in the symmetry plane for the fine case can be seen in Figure 18.

A drag reduction of **5.4 counts** using DES simulation was reached. The drag reduction is not as important as for the RANS simulation, a difference was expected as the two methods are very different. Recent work in the field assesses the benefits of using mean flow solutions of transient DES to improve the accuracy of the adjoint solution [12]. Running the Phase 2 “Front-to-rear” cases using a DES primal solution would add extra information to explain further the difference in drag reduction. In Figure 19, the evolution of the drag coefficient for both the coarse and fine cases is plotted for the original and morphed geometry over the 3.0 seconds of transient simulation time. Table 5 gives the drag coefficients obtained for each case with an average over the last 1.0 second on the fine case:

The development along the car of the lift and drag coefficients for the DES runs for the original and the morphed geometry is compared in Figure 20. As there is no porous media in this case there is no porous drag. The viscous drag is showing a slight decrease with a delta of 0.1698 counts while the pressure drag (focus of the optimization) shows a more significant drag reduction (-5.57 counts).

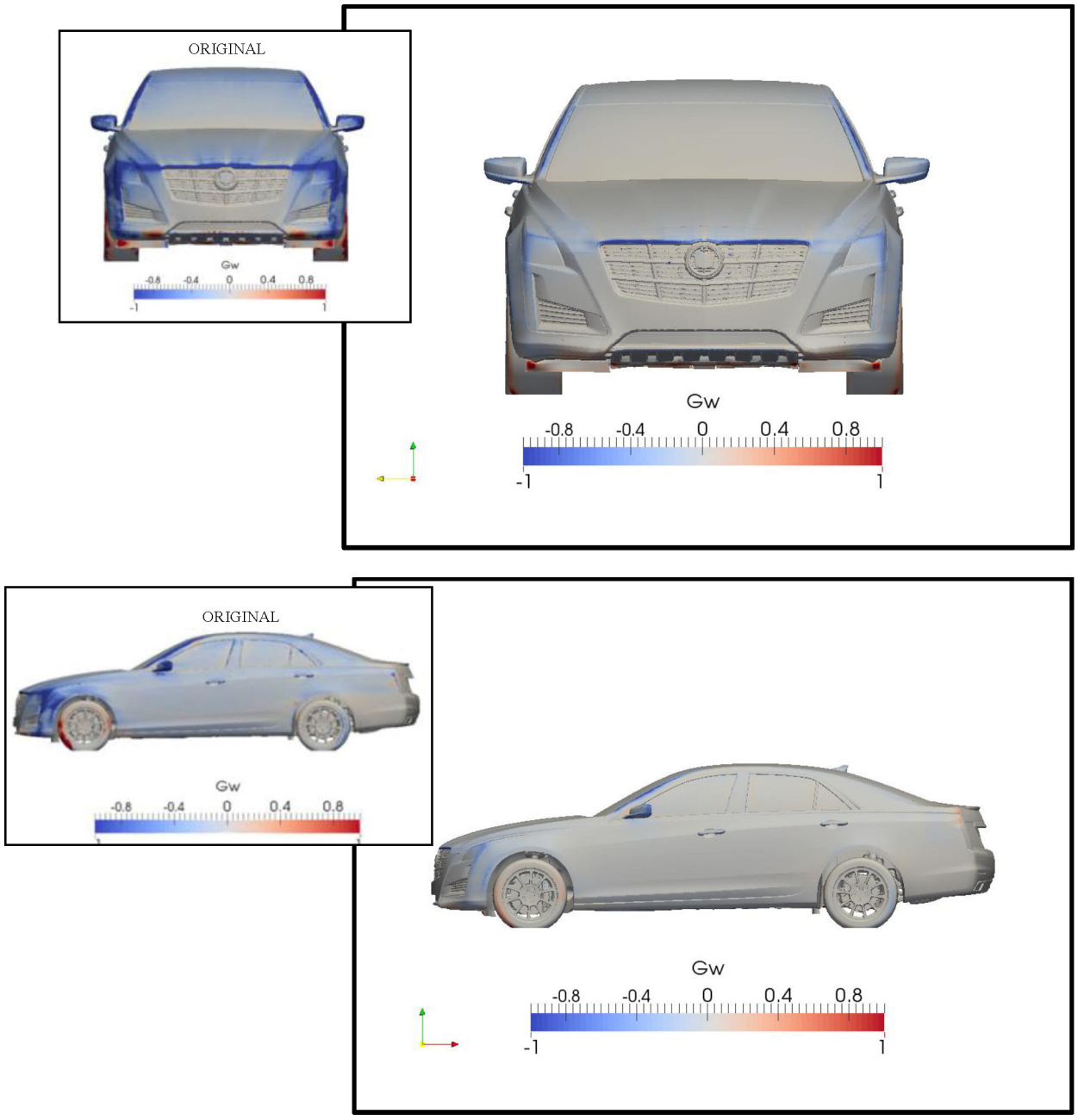


Figure 17. Comparison of sensitivities of the original (inset) and morphed geometry.

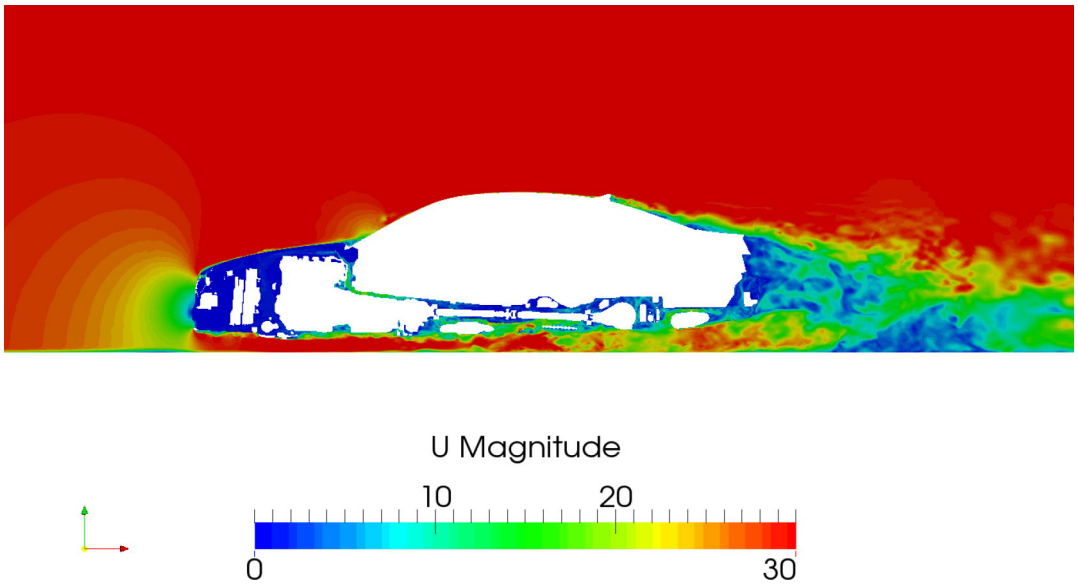


Figure 18. Original geometry: Instantaneous velocity field plot on y=0 cut after 3 seconds.

Table 5. Comparison of the DES run drag coefficient between the original and the optimized geometry

Case ID	Area modified	ΔCd accumulated (count)	Frontal Area (m^2)
Original	NA	-	2.3212
Optimized	All sub-regions	-5.4	2.3184

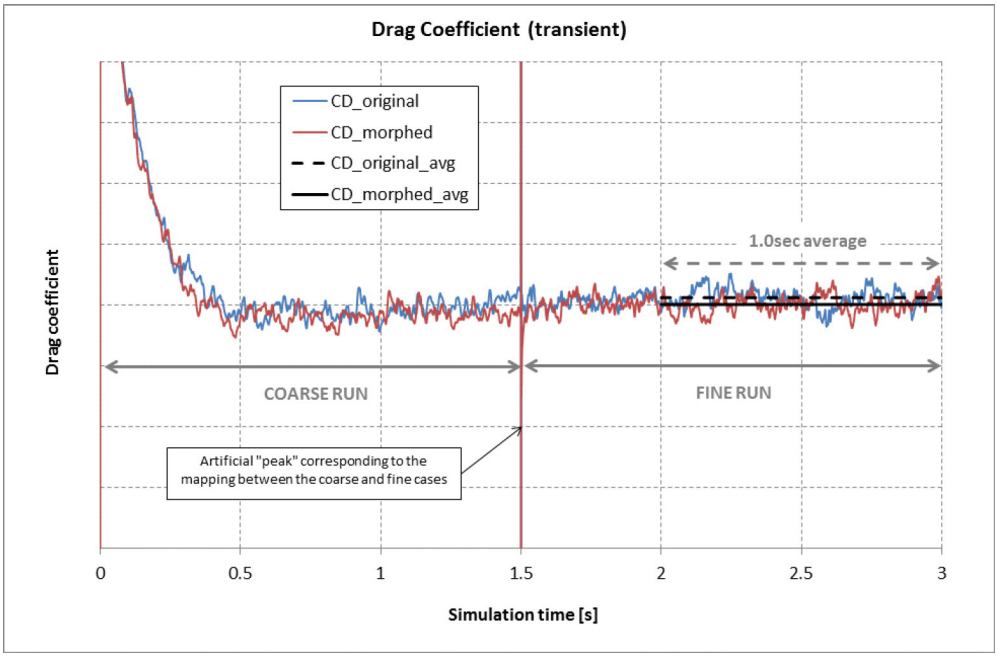


Figure 19. Drag coefficient evolution for the transient DES coarse and fine cases (original and morphed geometry)

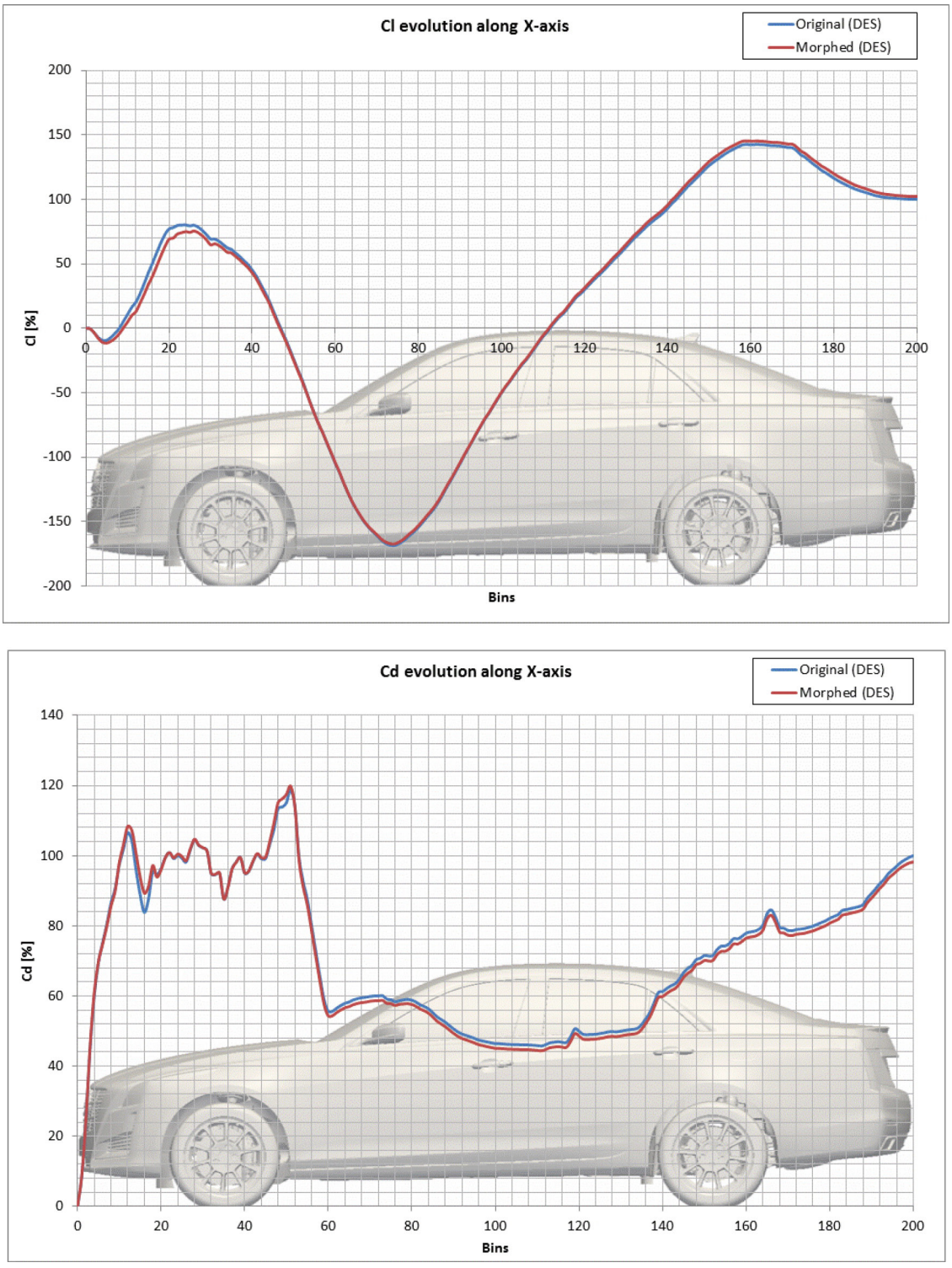


Figure 20. Lift (top) and drag (bottom) bin distribution comparison of the original and morphed geometry for the DES confirmation run.

SUMMARY

An adjoint-based vehicle shape improvement process for reduced drag was described. A traditionally optimized vehicle shape was chosen to assess the extra value of the proposed method. Optimization of the vehicle shape was attempted in two phases. In the first phase, an automated optimization method for the whole exterior surface of the vehicle was performed. The automated approach, using the sensitivity-based mesh morpher, imposes small iterative changes to the surface. Although the morpher includes a smoothing process, this approach was not able to provide an aesthetically pleasant surface mainly because of the noise in the computed sensitivities. The resulting surface can however be used as a valuable guide for the designer. In the second phase, six regions of high sensitivity areas were identified from the baseline vehicle simulations and a manual morphing was applied using morphing boxes around the sub-regions. This approach allowed for large shape changes, enforcement of the constraints and also provided smooth surfaces. Each sub-region design was evaluated and validated separately using a cumulative approach through which the previous sub-region shape changes were included in each new design.

The intermediate confirmation runs were performed with a Reynolds Averaging Navier Stokes (RANS) solver using the Realizable k-ε turbulence model. After completion of the 6th sub-region run, the total drag reduction reached 9.1 counts in this sequential process of primal-adjoint-morph loop. This proved to be a better approach, as it enabled larger surface deformations smoothly as opposed to the former automated approach. The DES confirmation run showed a drag reduction of 5.4 counts using this second approach. Further wind-tunnel testing using a reduced scale clay model will be reported in future publications. In future work an alternative approach using DES rather than RANS for the primal solution may allow for further reduction of the DES predicted drag.

REFERENCES

1. Jameson, A. *Aerodynamic Design via Control Theory*, *in ICASE Rep. no. 88-64*, 1988.
2. Giles, M.B. and Pierce N.A., *Adjoint Equations in CFD: Duality, Boundary Conditions and Solutions Behaviour*, in *AIAA Report 97-1850*, 1997.
3. Anderson, W.K. and Venkatakrishnan V., *Aerodynamic Design Optimizations on Unstructured Grids with a Continuous Adjoint Formulation*, in *AIAA Paper 97-0643*, 1997.
4. Petropoulou S., Localised Adjoint Optimization - Better and Faster CFD-Driven Design, NAFEMS Optimization for Industrial Applications Seminar, Gaydon, UK, March 2012.
5. Petropoulou S., Adjoint Solver Advances, Tailored to Automotive Applications, Flow head Conference, Munich, Germany, 28th March 2012.
6. Palluch J., Weickgenannt S., Saroch M. (Friendship Systems, GER), Leroy B., Zimmer A. (ICON, UK) Design Studies and Optimization of Functional Surfaces utilizing Open Source CFD, NAFEMS World Congress (NWC 2013), Salzburg, Austria, 10th June 2013.
7. iconCFD® version 3.0.17 Technical User Guide, ICON Technology & Process Consulting Ltd.
8. ANSA version 15.2.3 User's Guide, BETA CAE Systems S.A., January 2015.
9. Petropoulou S., Industrial optimization solutions based on OPENFOAM®* Technologies, ECCOMAS CFD, Lisbon, Portugal, June 2010.
10. Othmer, C., *A Continuous Adjoint Formulation for the Computation of Topological and Surface Sensitivities of Ducted Flows* Int J. Numer. Meth. Fluids, 2008. 58: p. 861-877.
11. Shih, T.-H., Liou, W.W., Shabbir, A., Yang, Z., Zhu, J., 1995. A New k- Eddy-Viscosity Model for High Reynolds Number Turbulent Flows - Model Development and Validation. Computers Fluids, 24(3): 227-238.
12. Blacha, T., Gregersen, M.M., Islam, M., Bensler, H., 2015. Aerodynamic Vehicle Optimization using the Continuous Adjoint Method. FKFS Conference, Stuttgart, Germany, 29th September 2015.

All rights reserved. No part of this publication may be reproduced, stored in a retrieval system, or transmitted, in any form or by any means, electronic, mechanical, photocopying, recording, or otherwise, without the prior written permission of SAE International.

Positions and opinions advanced in this paper are those of the author(s) and not necessarily those of SAE International. The author is solely responsible for the content of the paper.